Originally published as:

RESEARCH ARTICLE

Key Points:
- A piece of delaminated continental lithosphere is imaged beneath southern Puna
- A significant low-Q zone lies between the Nazca and South American lithosphere
- Lateral variations of the low-Q zone reflect the possible mechanism conversion

Correspondence to:
X. Liang,
liangxf@mail.iggcas.ac.cn

Delamination of southern Puna lithosphere revealed by body wave attenuation tomography

Xiaofeng Liang[1,2], Eric Sandvol[2], Suzanne Kay[3], Benjamin Heit[4], Xiaohui Yuan[4], Patrick Mulcahy[3], Chen Chen[3], Larry Brown[3], Diana Comte[5], and Patricia Alvarado[6]

[1]Institute of Geology and Geophysics, Chinese Academy of Sciences, Beijing, China, [2]Department of Geological Sciences, University of Missouri, Columbia, Missouri, USA, [3]Department of Earth and Atmospheric Science, Cornell University, Ithaca, New York, USA, [4]Deutsches GeoForschungsZentrum, Potsdam, Germany, [5]AMTC-Departamento de Geofisica, FCFM, Universidad de Chile, Santiago, Chile, [6]Departamento de Geofisicay Astronomía, CONICET, Universidad Nacional de San Juan, San Juan, Argentina

Abstract The southern Puna Plateau has been proposed to result from a major Pliocene delamination event that has previously been inferred from geochemical, geological, and some preliminary geophysical data. Seventy-five seismic stations were deployed across the southern Puna Plateau in 2007–2009 by scientists from the U.S., Germany, Chile, and Argentina to test the delamination model for the region. The Puna passive seismic stations were located between 25 and 28°S. Using the seismic waveform data collected from the PUNA experiment, we employ attenuation tomography methods to resolve both compressional and shear quality factors (Qp and Qs, respectively) in the crust and uppermost mantle. The images clearly show a high-Q Nazca slab subducting eastward beneath the Puna plateau and another high-Q block with a westward dip beneath the Eastern Cordillera. We suggest that the latter is a piece of delaminated South American lithosphere. A significant low-Q zone lies between the Nazca slab and the South American lithosphere and extends southward from the northern margin of the seismic array at 25°S before vanishing around 27.5°S. This low-Q zone extends farther west in the crust and uppermost mantle at the southern end of the seismic array. The low-Q zone reaches ~100 km depth beneath the northern part of the array but only ~50 km depth in the south. Lateral variations of the low-Q zone reflect the possible mechanism conversion between mantle upwelling related to delamination and dehydration. The depth of the Nazca slab as defined by Q images decreases from north to south beneath the plateau, which is consistent with the steep-flat transition of the angle of the subducting slab as defined by previous earthquake studies.

1. Introduction

The Central Andean plateau (Figure 1), which is extensively covered by volcanic rocks, was uplifted primarily by crustal thickening produced by horizontal shortening over a variably and relatively shallow dipping subduction zone [e.g., *Allmendinger et al.*, 1997; *Isacks*, 1988; *Kay and Coira*, 2009; *Oncken et al.*, 2006]. Overall, the mountain building can be attributed to strong coupling on the Nazca-South American plate interface and weak plastic yield strength of the overriding mantle wedge beneath the South American plate [e.g., *Isacks*, 1988; *Luo and Liu*, 2009]. Along-strike variations in the preexisting crustal and mantle lithosphere and in the angle of the Nazca plate have been suggested to have had a strong influence on north to south differences along the plateau in volcanic and deformational history, differential uplift and thinning and thickening of the underlying crust and mantle lithosphere [e.g., *Kay and Coira*, 2009; *Pilger*, 1981; *Tassara*, 2005]. Understanding the mountain building process of the Central Andean plateau, which can be divided into the Altiplano plateau to the north of 22°S and the Puna plateau to the south, should be a key to understanding Andean-type orogenic process. The focus of this study is to analyze the seismic attenuation images at the southern part of the Puna plateau in the region where it merges into the Chilean-Pampean flat slab to the south (Figure 1) and where the delamination of Andean crustal and mantle lithosphere was first proposed [*Kay and Kay*, 1993; *Kay et al.*, 1994].

The Puna plateau itself is divided into the northern and southern Puna near 24°S [see review in *Allmendinger et al.*, 1997]. The southern Puna plateau in the southernmost part of the Central Andean Puna-Altiplano plateau contains the southernmost portion of the Central Andean Volcanic Zone arc segment (CVZ), which like the plateau terminates as the subducting slab shallows into the Chilean-Pampean flat-slab region at the latitude of the Andean back-arc Sierras Pampeanas ranges [*Cahill and Isacks*, 1992; e.g., *Jordan et al.*, 1983].
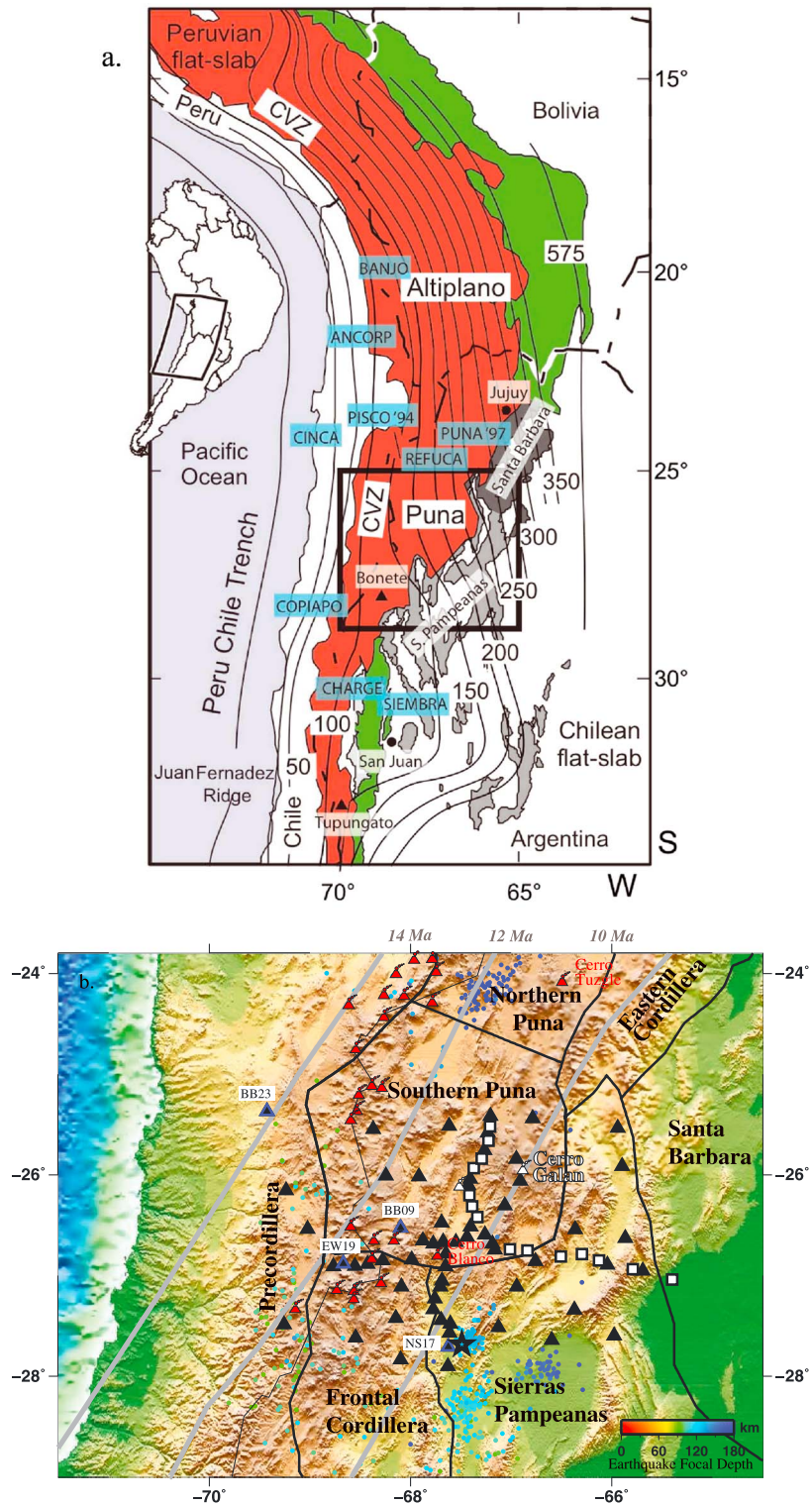
Figure 1. (a) Location of the southern Puna within the Central Andes. The black rectangle shows the range of the PUNA array. The depth contours to the Benioff zone of the subducted Nazca slab from *Mulcahy et al.* [2010] are plotted as thin black lines with 25 km interval. CVZ: central volcanic zone. (b) Location of PUNA experiment and the deep seismicity used in this research. The positions of the Juan Fernandez ridge at different times (0, 10, 12, and 14 Ma) are shown as grey lines [*Yáñez et al.*, 2001]. The seismicity is from the catalogue located using PUNA data [*Mulcahy et al.*, 2010] and color coded by depths. The short-period stations are shown as open squares and the intermediate and broadband stations are shown as filled triangles. Volcano locations are from global volcanism program of the Smithsonian Institution. Cerro Galan and Cerro Blanco are marked with white and red volcano symbols, respectively. The black star shows the location of the earthquake used in Figure 2. The black triangles with blue frame and station names are the stations used in Figure 2.

The southern Puna itself is characterized by many unique geological and geochemical features with respect to the rest of the Puna plateau, including eruption of post late Miocene intraplate and back-arc calc-alkaline lavas [*Kay et al.*, 1994] and the giant 6.5 to ~2 Ma back-arc Cerro Galán ignimbrite [*Folkes et al.*, 2011; *Kay et al.*, 2011, 2010; *Sparks et al.*, 1985] in association with a distinctive contemporaneous stress system involving thrust, strike slip, and normal faulting [*Marrett et al.*, 1994]. In contrast, the northern Puna is essentially devoid of similar mafic magmas, where the largest back-arc ignimbrite eruptions erupted before 6.5 Ma and the stress system is largely compressive [*Coira and Kay*, 1993; *Coira et al.*, 1993; *Kay et al.*, 2010].

The distribution and chemistry of young basaltic to mafic andesitic volcanic rocks erupted in the southern Puna plateau provide important clues to lithospheric and asthenospheric processes east of the main volcanic front of the CVZ. Based on the discussion in *Kay et al.* [1994], there are three major groups of young mafic volcanic lavas on the Puna plateau. The first is an intraplate group, which occurs over a thin continental lithosphere above an intermediate seismicity gap in the subducting plate in the southern Puna and represents the highest percentage of mantle partial melt. The second is a high-K calc-alkaline group, which erupted over an intermediate thickness lithosphere on the northern and southern margins of the seismic gap and behind the frontal arc, and represents an intermediate percentage of mantle partial melt. In contrast, the third group in the northern Puna and Altiplano consists largely of small-volume shoshonitic lavas that formed by very small percentages of mantle partial melt and erupted through a relatively thick continental lithosphere [*Coira and Kay*, 1993; *Davidson and Silva*, 1995]. These volcanic groups reflect the different lithospheric structures beneath the Central Andean plateau.

A major Pliocene delamination event in the southern Puna was inferred by *Kay et al.* [1994] based on the observations listed above and the criterion enumerated below. The first of these criteria was the high elevation and relatively flat surface of the Puna plateau, which *Isacks* [1988] had argued required a thermal component to explain its high elevation. This was also one of the criteria used by *England and Houseman* [1989] and *Molnar et al.* [1993] to argue for lithospheric delamination below the Tibetan Plateau. Earlier geophysical and geothermal studies had called upon an unusually thin crust and a very hot mantle to explain the characteristics of this region [e.g., *Febrer et al.*, 1982]. The second criterion was the seismic wave attenuation studies of intermediate-depth earthquake raypaths by *Whitman et al.* [1992], which showed strong along-strike differences with the central plateau and marked attenuation beneath the southern Puna. These observations were used to suggest a very low Q zone in the asthenospheric wedge above the subducted slab and a thinner continental mantle lithosphere beneath the southern than the northern Puna [*Whitman et al.*, 1992, 1996], which was later reinforced by studies by *Schurr et al.* [2003, 2006] in the northern Puna. Farther north over the steeper subducting slab in the Puna and the Altiplano around ~21°S, a strong localized low velocity and Q anomalies in the upper mantle back-arc lithosphere have been attributed to partial melting associated with a gap in the continental mantle lithosphere [*Beck and Zandt*, 2002; *Heit et al.*, 2008; *Myers et al.*, 1998]. A third criterion for delamination was the fault kinematics analysis of Mio-Pliocene deformation in the Puna and adjacent foreland performed by *Allmendinger* [1986] and *Marrett et al.* [1994], which indicated a change in the regional stress distribution that is now argued to have been initiated at ~7 Ma [e.g., *Risse et al.*, 2008]. A fourth set of criteria were the geochemical variations in southern Puna plateau mafic lavas discussed above, the presence of glassy andesites to dacitic lavas and young ignimbrites, and the suggestion that the intraplate like lavas reflect decompression melting in a hot mantle wedge [*Kay et al.*, 1994]. The final criterion is the gap of intermediate depth slab seismicity in the subducting slab between 25.5°S and 27.5°S [e.g., *Cahill and Isacks*, 1992; *Mulcahy et al.*, 2010] which *Kay et al.* [1994] attributed to a hot mantle wedge.

The southern part of the region studied here also straddles the northern boundary of the Chilean-Pampean flat-slab region, whose origin is commonly associated with the subduction of the Juan Fernandez aseismic oceanic plateau on the Nazca plate [e.g., *Anderson et al.*, 2007; *Yáñez et al.*, 2001]. Evidence for a role of this ridge subduction comes from the subduction of the ridge coinciding spatially with the gap in arc volcanism and temporally with the timing of the shallowing of the flat slab as inferred from magmatic and geologic criteria [e.g., *Kay and Abbruzzi*, 1996; *Kay and Mpodozis*, 2002; *Ramos et al.*, 2002]. Enhanced seismic activity in the region and various topographic effects have led many to suggest the shallow dip of the slab is the result of the positive buoyancy of the plateau or ridge imbedded in the oceanic lithosphere [e.g., *Alvarado et al.*, 2009; *Pilger*, 1981]. The gap in active volcanism across the flat-slab region is attributed to the dip of the subducting slab being so shallow that effectively no asthenospheric wedge exists to produce arc volcanism [e.g., *Barazangi and Isacks*, 1976]. The reconstructed Juan Fernandez ridge has a northeast trending arm

linked to the nearly east–west segment that began to subduct under the Chilean-Pampean flat-slab region at circa 10 Ma [*Yáñez et al.*, 2001]. The southward subduction of the kinked Juan Fernandez ridge has been suggested to be linked with a southward shallowing of the subducting slab, which is reflected in the late Neogene volcanic activity on the Puna plateau can account for the volcanism activities of Altiplano-Puna [*Kay and Coira*, 2009]. With the passing of the northeast trending arm of the ridge beneath the southern Puna at ~7 Ma, the slab is argued to have started to resteepen as lithospheric delamination initiated as reflected by the giant eruptions of the Cerro Galán ignimbrites at ~7.5–2 Ma, mafic magma eruptions, and the change in deformation pattern. Continued southward subduction of the ridge would be expected to produce a southward pattern of steepening, which initiated after the Pliocene at the southern end of the Puna plateau [*Kay et al.*, 2013].

A low-viscosity wedge may produce a flat-lying slab beneath an overriding plate, and the transition of a subduction zone into a flat-lying regime could be preceded by changes in the amount of volatiles such that the dehydration front moves to shallower depths [e.g., *Manea and Gurnis*, 2007]. The amount of mantle melt is primarily governed by temperature and hydration, and thus a lack of volcanism may be explained by anomalously low temperatures and/or by inadequate water flux [e.g., *Stachnik et al.*, 2004]. Alternatively, partial melt that has not yet reached the surface could exist at depth. In a shallow subduction regime, the slab dewatering process could become slow with gradual hydration of the overlying mantle [*Porter et al.*, 2012] or the shallow subducting angle may produce a lower slab temperature and delay the dehydration reactions within the subducted slab [e.g., *Manea and Manea*, 2011].

2. Data and Method

The PUNA or PUDEL (PUna DELamination) passive seismic experiment was operated from 2007 to 2009 across the southern Puna plateau in an area bounded by 25–28°S and 70–65°W (Figure 1b). This 75-station experiment was a collaboration of Argentine, Chilean, German, and U.S. scientists. The U.S. component of the network included 23 broadband and 22 intermediate-period seismometers (PUNA) and the German component included 16 broadband and 14 short-period seismometers (PUDEL).

In this paper, we use attenuation tomography to resolve both the compressional and shear quality factors (Qp and Qs) in the crust and uppermost mantle. Following the approach outlined by *Scherbaum* [1990], the observed amplitude spectrum of the event i at station j can be described as

$$A_{ij} = S_i(f)I_j(f)R_j(f)B_{ij}(f), \qquad (1)$$

where f is frequency, S is the source spectrum, I is the instrument response, R is the local site amplification, and B is the absorption along the raypath from the event i to station j.

The far-field source amplitude spectrum can be modeled as

$$S_i(f) = \Omega_0 \frac{f_c^\gamma}{f_c^\gamma + f^\gamma}, \qquad (2)$$

where Ω_0 is the long-period amplitude value, f_c is the source corner frequency, and γ is the high-frequency decay rate. A Brune-type source model is equivalent for $\gamma = 2$ [*Brune*, 1970].

The attenuation spectrum is

$$B_{ij}(f) = e^{\frac{-\pi f s}{vQ}} = e^{\frac{-\pi f t}{Q}} = e^{-\pi f t^*}, \quad \text{where} \quad t^* = \frac{t}{Q}. \qquad (3)$$

Here t is the traveltime corresponding to the raypath length s and velocity v, Q is the quality factor, and f is the frequency of seismic waves. Based on equation (3), t^* measurements embed the influence from velocity variations. Velocity perturbations are usually 1 order smaller than Q perturbations, so the influence of velocity variations is minor for t^* measurements in a region with strong Q variations.

When a Brune source model is assumed, the velocity amplitude spectra for an f^2 source model assuming whole path attenuation are

$$A(f) = 2\pi f \Omega \frac{f_c^2}{f_c^2 + f^2} e^{-\pi f t^*}, \qquad (4)$$

where Ω is the spectral level, which reflects the factors which will change the amplitude of seismic waves, including site amplification, radiation pattern and source moment. This model does not include frequency-dependent

site amplification and uses a simple f^2 source spectrum, consistent with most previous studies [e.g., *Eberhart-Phillips and Chadwick*, 2002; *Scherbaum*, 1990]. To determine the parameters, all spectra for the same event are jointly inverted for the same corner frequency f_c, and different spectral level Ω and t^* for each path. Equation (4) can be rewritten as

$$\ln\{A(f)\} = \ln\{2\pi f\Omega\} - \ln\left\{1 + (f/f_c)^2\right\} - \pi f t^*. \tag{5}$$

The unknowns in this equation are $\ln\{2\pi f\Omega\}$, corner frequency f_c, and t^*. The corner frequency f_c of each event is estimated by using a grid search over the frequency range 0.05–20 Hz for all of the recorded waveform at each station for each event and then taking the average of all the best fitting f_c for each record. Once f_c is determined, the remaining linear equation (5) is solved for $\ln\{2\pi f\Omega\}$ and t^* by least squares regression. We observed a clear linear relation between the corner frequency and magnitude from both of our estimations of corner frequency for *P* and *S* waves (see Figure S1 in the supporting information).

The physical mechanisms of attenuation can potentially be discriminated by their frequency dependence, described by

$$t^* = t_0^* f^{-\eta}, \tag{6}$$

where t_0^* represents attenuation at 1 Hz [*Stachnik et al.*, 2004] and η is the frequency dependence parameter. Here we apply a least squares regression of t^* including frequency dependence. We use a grid search for η from −1.0 to 1.0 with a step of 0.02.

Using the newly collected seismic waveform data from the southern PUNA or PUDEL project [see *Bianchi et al.*, 2013], we analyze the body wave spectra of local and regional earthquakes for *P* waves using vertical component waveforms and for *S* waves using transverse component waveforms, respectively. There are 1072 earthquakes located using the PUNA array with a residual less than 1 s and recorded by more than four stations [*Mulcahy et al.*, 2010]. Here we only pick arrivals from the earthquakes with focal depths greater than 90 km to avoid the phases *Pn* and *Sn*. There are 521 deep earthquakes used here and most of them are located to the north, west, and east of the array (Figure 1b). The instrument responses are removed from the original data and then the horizontal components rotated to radial and transverse components. Then a 3 s window is cut from the start of the phase as signal, and another 3 s window before the start of the phase is cut as noise. We calculated the multitaper spectra [*Park et al.*, 1987] for the corresponding signals and noise using a 3 s duration (Figure 2). The useful frequency band for computing t^* is selected based on the signal-to-noise ratio (SNR) being above a threshold of 3.0 over a given frequency range. Following *Wang et al.* [2010], the data quality index (QI) has been used to ensure the quality of the inversion for *Q*. The QI is assessed by two factors: the signal/noise index, based on the percentage of the high SNR data in the entire fitting spectra, and the amplitude spectra misfit factor. The QI is used to select the data with at least 60% of signal with a SNR higher than 3 and give the weight of the t^* in the inversion. Overall, there are 18,048 *P* wave t^* measurements and 2487 *S* wave t^* measurements used in the inversion.

The SIMUL2000 tomography code (http://www.geology.wisc.edu/~thurber/simul2000/) is used to do the *Q* inversion [*Thurber and Eberhart-Phillips*, 1999]. There are $25 \times 25 \times 20$ model grids for a space of $1600\,km \times 1600\,km \times 800\,km$ along the longitude, latitude, and depth dimensions with center at 27.5°S, 67.5°W. The model grids are set to different sizes according to the distance from the model center; in addition, the grid size becomes smaller from the model edges to the model center. The largest grids have a length of 200 km at the edges of the model space. The medium ones have a length of 60 km around the research region. The smallest ones have a length of 20 km in the center of the model space. To eliminate the potential influence for t^* from the velocity variation, we use the *P* wave tomographic results from *Bianchi et al.* [2013] as the reference model for *P* wave ray tracing. At the same time, we calculate a 1-D average *P* wave velocity (*Vp*) model based on this 3-D *Vp* model and convert it to a 1-D *S* wave velocity (*Vs*) reference model using a constant *Vp*/*Vs* of 1.78 for *S* wave ray tracing.

Using this method, the magnitude of the events does not affect the shape of the velocity spectra from which we get t^* by regression. We checked a series of events with different magnitude and the t^* measurements from these events show no consistent magnitude versus t^* values relationship (Figure 3). The resolution tests show well-recovered input checkerboard anomalies for the upper 150 km depth (Figures 4 and 5) along the cross sections that are used to present our tomographic images. There is strong smearing along the north–south direction as well as outside of the array, because there are more raypaths with a north–south trend for
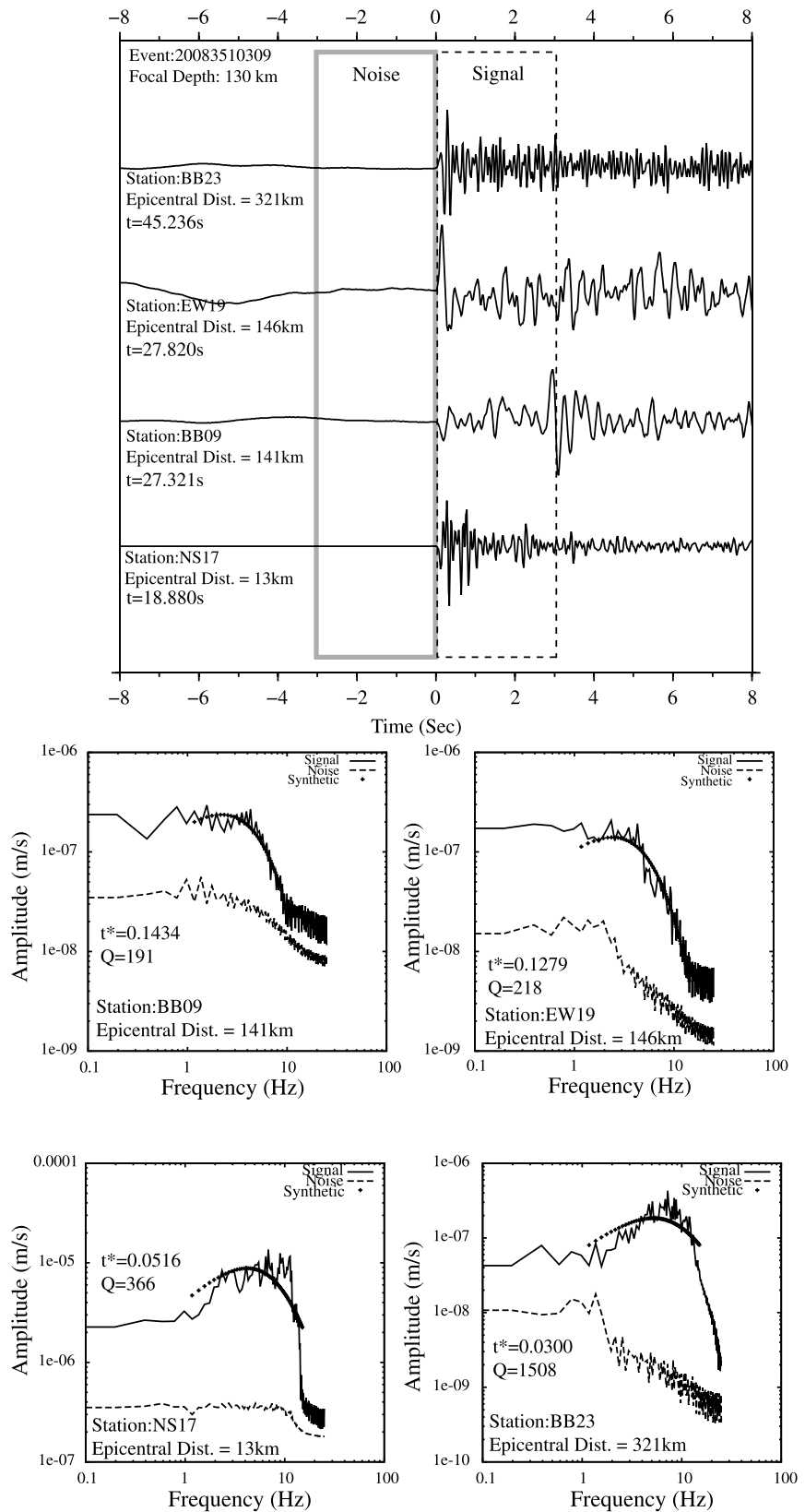
Figure 2. Four waveform examples and their corresponding amplitude spectra. The amplitude spectra and corresponding *t** measurements and estimated *Qp* along the raypath clearly show the different attenuation along the different raypaths. All four stations used are broadband seismometer: NS17-CMG-40T, BB09-CMG-3T, EW19-Trillium-40s, and BB23-Trillium-120s.
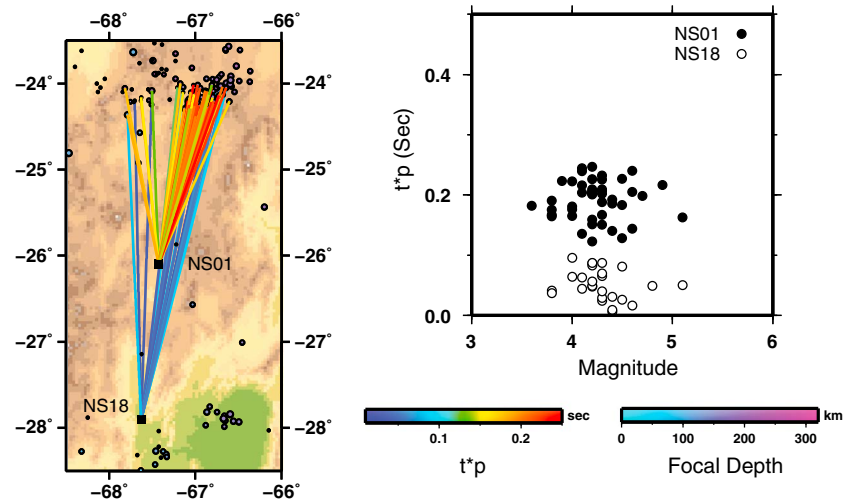
Figure 3. The collection of t^* measurements from the close earthquakes with different magnitudes to two stations shows no obvious relation between magnitude and t^*.

the earthquakes outside of the array (Figure 1). At the same time, the resolution for the model deeper than 150 km is also limited by the earthquake distribution, since the seismicity is scattered along the subducting slab. Since the effective S wave ray coverage is pretty uneven in the studied area, the resolution tests for S wave data are not performed.

3. Results

3.1. Tomographic Images

The tomographic images clearly show a high Qp and Qs anomaly that dips eastward and correlates with the Wadati-Benioff zone (Figures 6–8), and thus we interpret these high-Q zones as the Nazca slab subducting eastward beneath the Puna plateau. A second prominent feature is another high Qp block with a westward dip beneath the Eastern Cordillera (Figure 6, sections A-A' and D-D'). Linking these high Qp and Qs results with previous geophysical [*Whitman et al.*, 1992, 1996] and geochemical observations [*Kay et al.*, 1994], we suggest that this westward dipping high-Q block indicates the presence of a piece of delaminated South American continental lithosphere. These same high-Q zones can be seen in the E-W trending Qp and Qs images in Figure 6 and in the Qp horizontal slices in Figure 8.

A zone of very high attenuation in the crust and uppermost mantle is seen beneath and west of Cerro Galán region (Figure 6, sections A-A' and B-B'; Figure 7, section H-H'; Figure 8). This attenuation is so strong that the S waves are totally blocked for the raypaths going through this part of the lithosphere as well as the crust and uppermost mantle (Figures 6 and 7). As such, we were unable to pick S phases to measure t^* for inverting the Qs for these raypaths (Figures 6 and 7). This extensive and extreme low-Q zone might reflect asthenospheric upwelling after the continental lithosphere delaminated in association with slab steepening as argued by *Kay and Coira* [2009]. This low-Q zone extends farther north approaching the region of the Cerro Tuzgle volcano (marked as a reference for this anomaly in Figure 8). As Cerro Tuzgle is outside of our array, we lack sufficient resolution to confirm the presence of the low Q feature in this region. However, velocity and attenuation tomographic studies [*Bianchi et al.*, 2013; *Schurr et al.*, 2006] show that the low velocities and low Q related with this volcano can be interpreted as being related to lithospheric delamination in this region as is also consistent with inferences from geochemical studies of the Cerro Tuzgle lavas [*Coira and Kay*, 1993].

Another distinct low-Q zone characterizes the region of the South American lithosphere above the Nazca slab from the northern margin of the array at 25°S to around 27.5°S, where it vanishes (Figure 6). As seen in the map view and sections, this low-Q zone extends farther to the west in the crust and uppermost mantle at the southern end of the array producing a "J" shape. The western high-Q region in the upper to middle crust underlies the potentially active ignimbrite dome complex of the Tres Cruces Massif in the west and the active Ojos del Salado volcanic complex just to the east [e.g., *Gardeweg et al.*, 2000; *Kay et al.*, 2013]. The flat segment
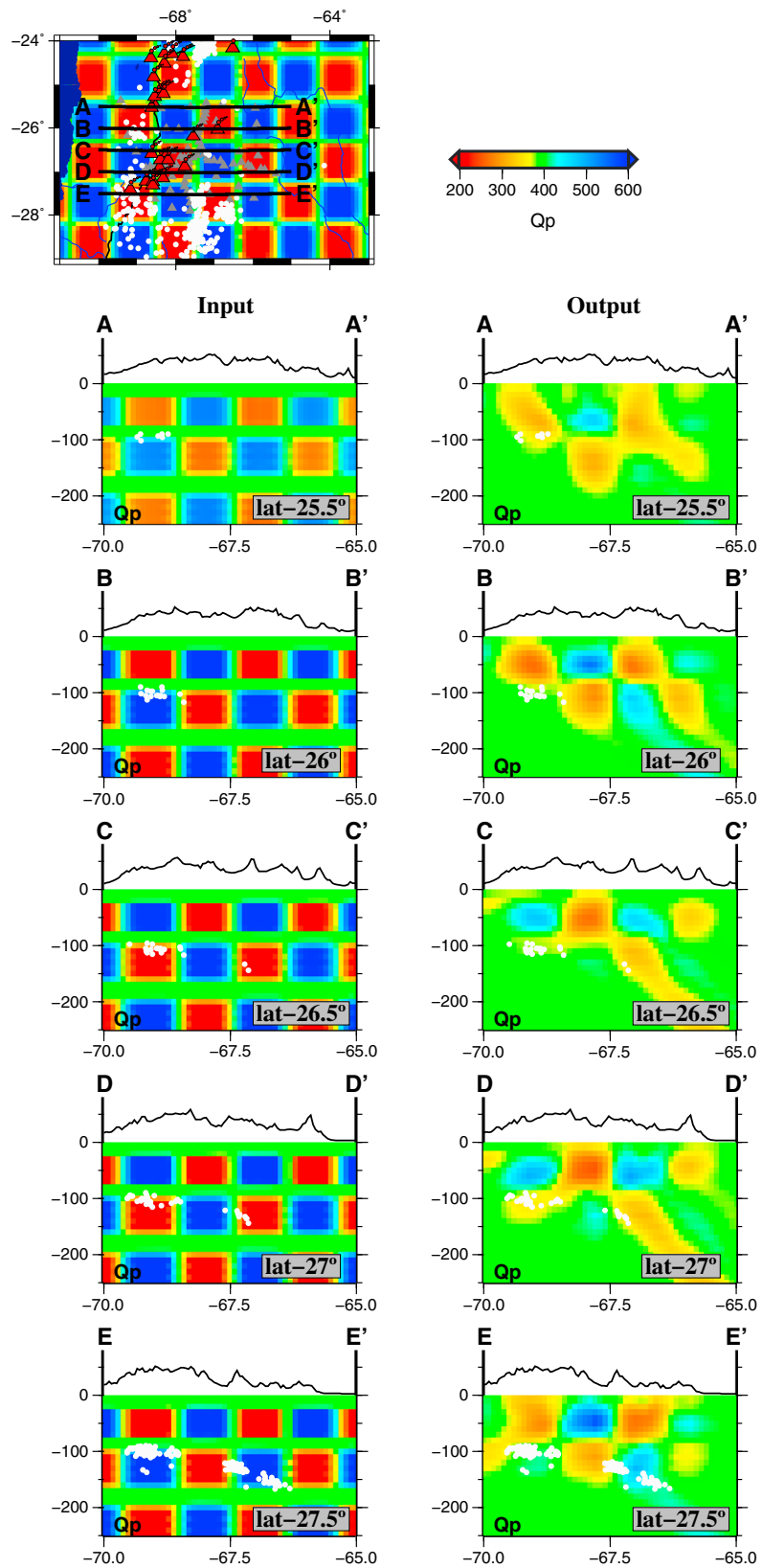
Figure 4. Resolution tests along the east–west cross sections. The input checkerboard is 90 km × 90 km × 60 km in the north–south, east–west, and depth dimensions. The figure demonstrates that the resolution is good in the upper 150 km, but the resolution for the lower part of the model is poor due to the seismicity distribution. The white dots are the seismicity within 50 km along the cross section.
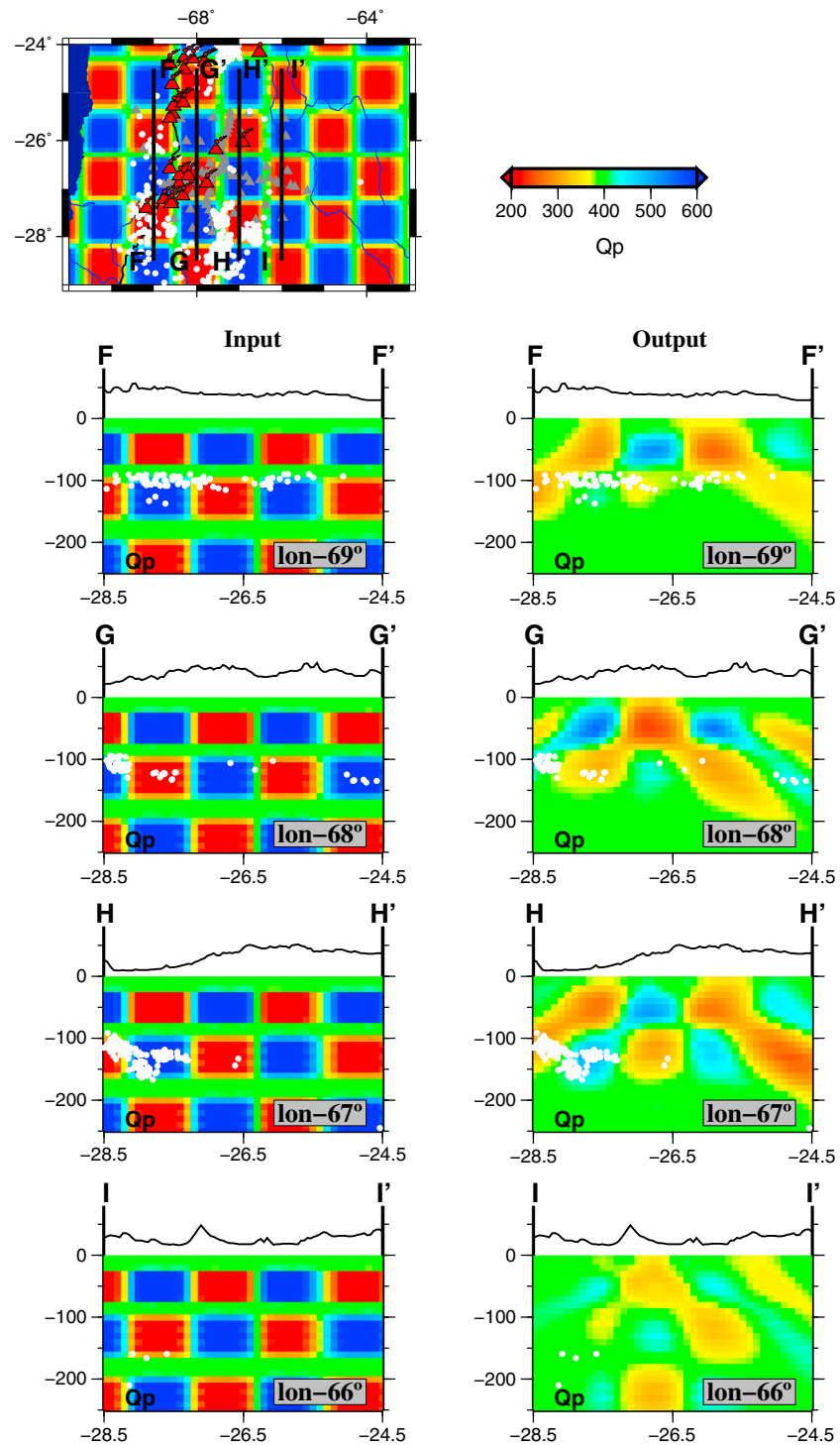
Figure 5. Resolution tests along the north–south cross sections. The figure demonstrates that the resolution is good in the upper 150 km, whereas smearing occurs outside of the array due to an uneven event distribution along the north–south direction. The white dots are the seismicity within 50 km along the cross section.

of the low-Q zone, whose top is at about 40 km depth, underlies the string of domes and small centers in the Cordillera de Buenaventura, one of which overlies a seismic swarm observed under the Cerro Torta dome in the time of the deployment of the PUNA array [*Mulcahy et al.*, 2010]. The eastward extension beneath the Salar de Antofalla corresponds with the regions of young mafic centers just west and southwest of the Cerro
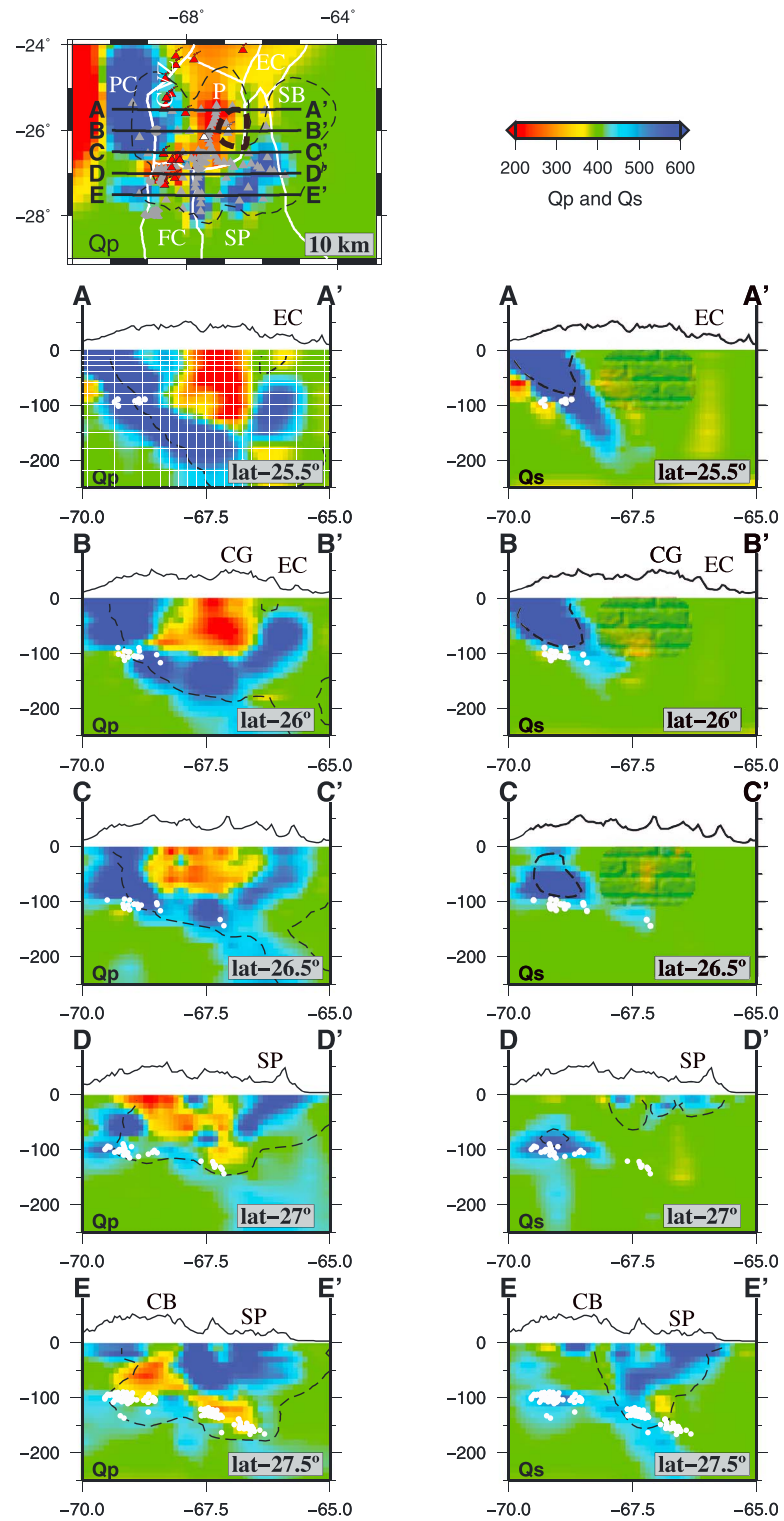
Figure 6. Vertical slices for both *Qp* and *Qs* tomographic results. Both sets of images from west to east show a clear transition from north to south. The shaded blocks show where the *S* phases are blocked. The dashed lines show the contour of hit count equal to 10. The positions of the vertical slices are shown on the top map view of 10 km depth *Qp* image. The white circles show the seismicity located by the PUNA array within 50 km along the cross sections [*Mulcahy et al.*, 2010]. The thin white mesh on A-A' shows the model mesh used in the inversion, which is the same for all cross sections. CB, Cerro Bonete-Nevado Pissis volcanic center; CG, Cerro Galán volcanic center. The thick dashed lines on the 10 km slices show the location of the Cerro Galán ignimbrites and the solid white lines separate the geologic units following Figure 1: P, Puna; EC, Eastern Cordillera thrust belt; SB, Santa Barbara System inverted thrust belt; PC, Principal Cordillera; FC, Frontal Cordillera; SP, Sierras Pampeanas.
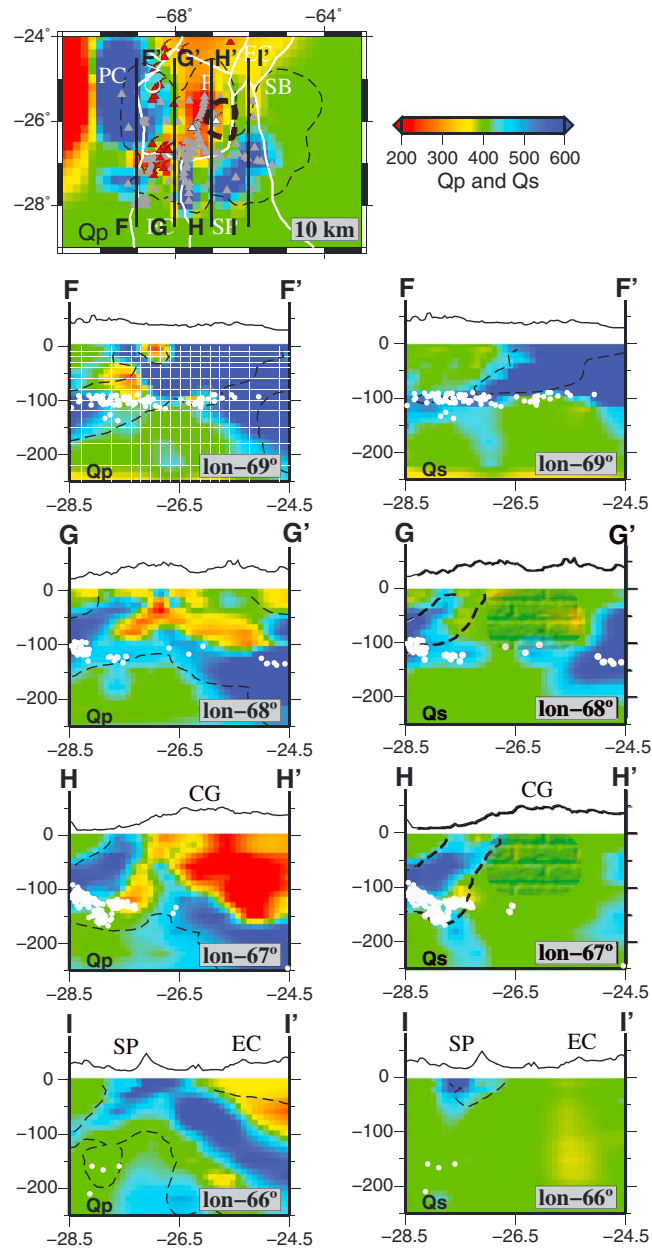
Figure 7. Vertical slices for both *Qp* and *Qs* tomographic results. Both sets of images for north to south sections of *Qp* and *Qs* show a clear transition from north to south. The shaded blocks show where the *S* phases are blocked. The dashed lines show the contour of hit count equal to 10. The positions of the vertical slices are shown on the top map view of 10 km depth *Qp* image. The white circles are showing the seismicity located by the PUNA array within 50 km along the cross sections [*Mulcahy et al.*, 2010]. The thick dashed lines on the 10 km slices show the location of the Cerro Galán ignimbrites and the solid white lines separate the geologic units following Figure 1. The thin white mesh on F-F' shows the model mesh used in the inversion, which is the same for all cross sections.

Galán area as does the underlying high attenuation zone over the slab. The absence of a high-*Q* zone in the CVZ arc region east of Cerro Galán at 25.5 to 26°S corresponds with a lack of very recent volcanic activity in the arc. The low high-*Q* zone in the lowermost crust and mantle above the slab near the arc region in the 27.5°S section (Figure 6, section E-E') lies just north of the Bonente-Incapilla volcanic complex region labeled CB, whose youngest dated activity is 0.5 Ma [*Goss et al.*, 2009]. The small finger toward the surface underlies the recently active Cerro Tipas center.

Overall, the low Q zone extends for about ~100 km in depth from the slab to the surface beneath the northern part of the array (Figure 6 sections A-A' to D-D'), whereas it only occurs over a depth of ~50 km or
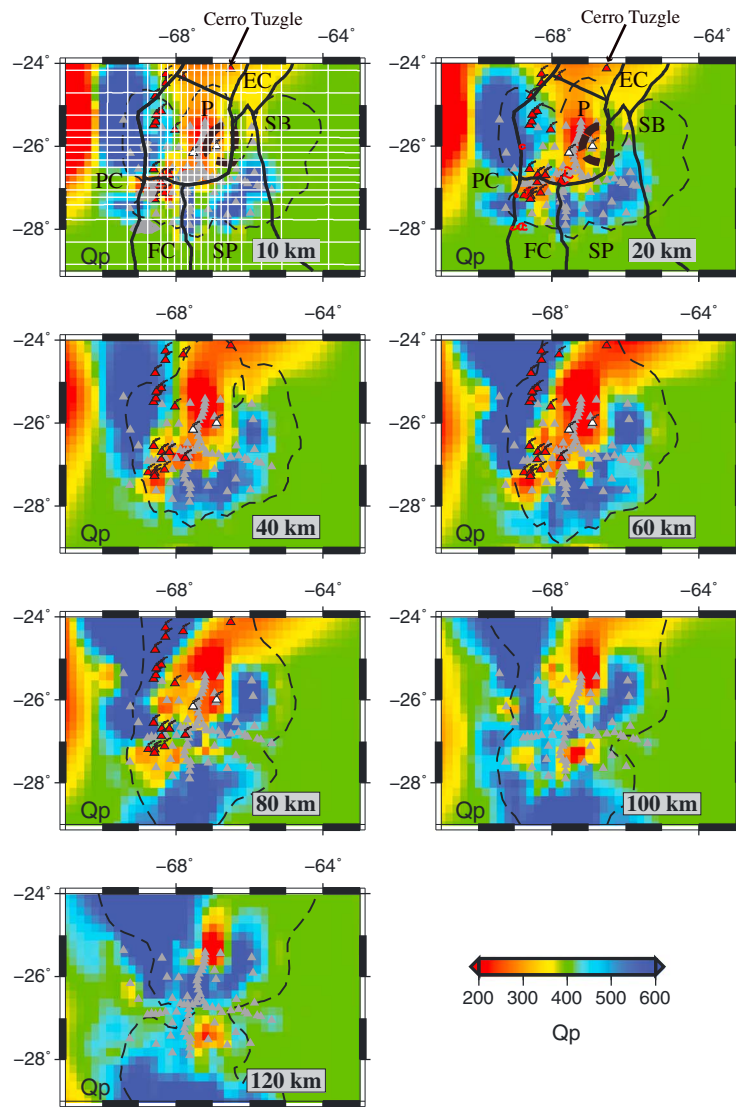
Figure 8. Horizontal slices for the Qp tomographic results at depths of 10, 20, 40, 60, 80, 100, and 120 km. The dashed lines show the contour of hit count equal to 10. The thick dashed lines on the 10 and 20 km slices show the location of the Cerro Galán ignimbrites and the solid black lines separate the geologic units following Figure 1. The thin white mesh on 10 km slice shows the model mesh used in the inversion, which is the same for all cross sections.

less above the slab in the south (Figure 6). The north–south lateral thinning of the low-Q zone is significant: from a very large region with low Q encompassing most of the mantle wedge beneath Cerro Galán, to a moderately thin low-Q layer overlying the slab beneath the southern end of the array where the slab shallows. At the southern end, both sides of the thin low-Q zone have uniformly high-Q values, which are best explained respectively as the subducted Nazca oceanic lithosphere and the South American continental lithosphere. Farther south, the slab is considered to directly underlie the continental lithosphere with little asthenospheric wedge in between [e.g., *Kay and Abbruzzi*, 1996; *Porter et al.*, 2012; *Smalley and Isacks*, 1987]. Given the lack of volcanism at the southern end of the PUNA array (i.e., in the flat-slab region), we attribute the thin low-Q layer to a region of concentrated water content and possibly to the initiation of melting of the mantle wedge. The northward lateral variation of the low-Q zone might reflect a conversion in mechanism from mantle upwelling and partial melting in the wedge following delamination in the north to slow slab dehydration, along the transition zone in which the dip of the subducted Nazca slab changes from normal to flat.

A custom resolution test has also been performed to check the reliability of the inverted Qp features (Figure 9). The three input features were used including a strong low Qp zone beneath the Cerro Galán
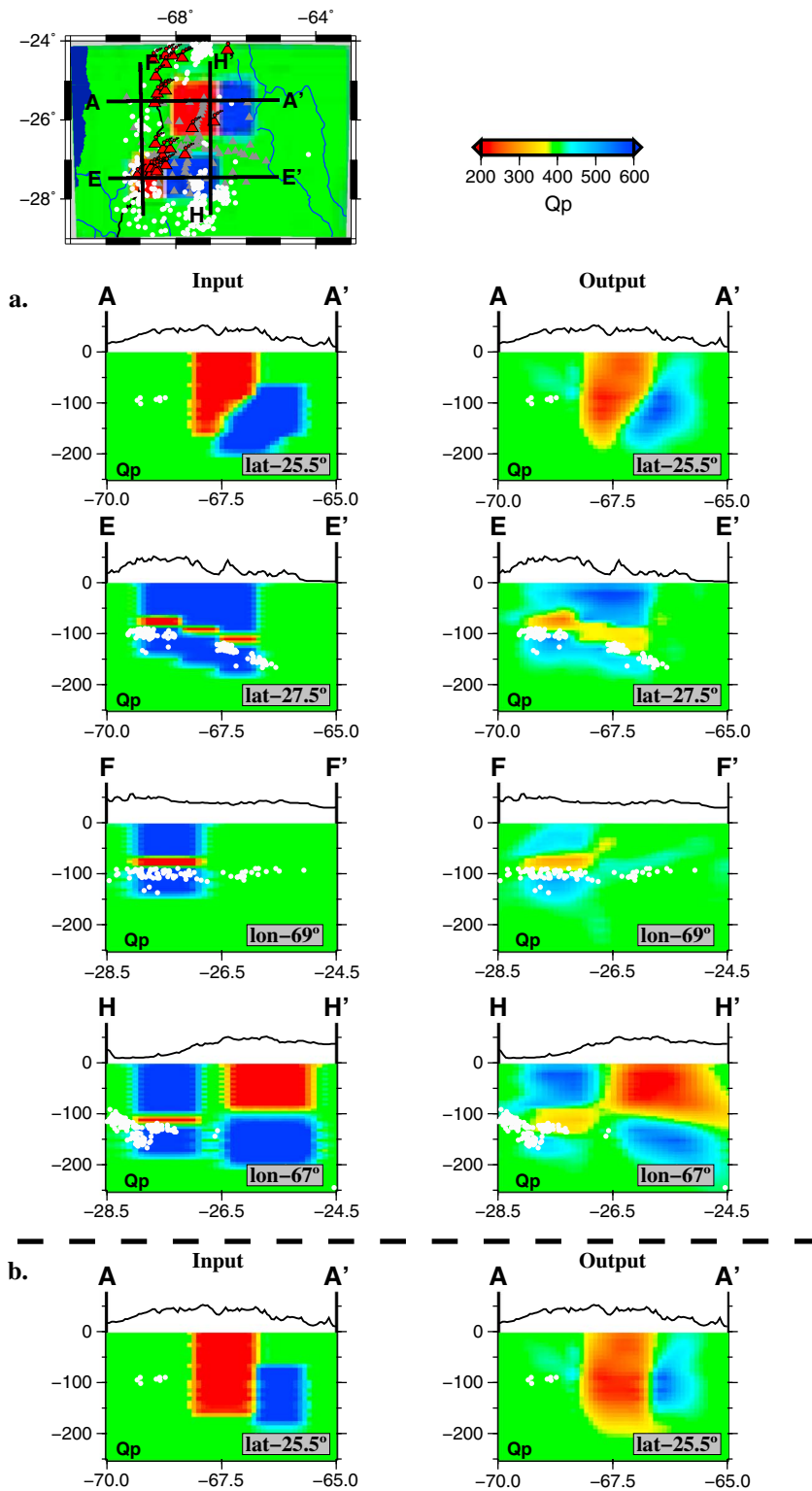
Figure 9. Two customized resolution test with five input anomalies representing the low Qp zone beneath the Cerro Galán ignimbrites, the high Qp zone interpreted as a piece of delaminated south American lithosphere, and the thin low Qp layer bounded by the high-Q subducting slab and overlain high-Q continental lithosphere. For test (a) using a westward dipping high Qp zone as the delaminated block, and for test (b) using a vertical extending high Qp zone instead of the westward dipping one.

region, a westward dipping (or vertical) high Qp zone adjacent to this low Qp region on its eastern side, and a thin low Qp zone with a thickness of 20 km to represent the inverted low Qp zone sitting above the slab. All three features are appropriately recovered in the resolution test except for the region outside of the array where strong smearing occurs in the checkerboard tests shown in Figures 4 and 5.

3.2. Frequency Dependence

In this study, we also used a grid search approach to estimate the influence from frequency dependence effects of quality factors (see supporting information). Over the typically observable frequency range of 2–20 Hz, a frequency dependence of 0.3 would make <10% difference in the amplitude decay compared to frequency in-dependence, and the frequency-dependent Q values will be about 60% of the frequency-independent Q values [*Eberhart-Phillips and Chadwick*, 2002]. Studies that solve for 3-D Q with a range of η find that the resulting Q models are similar and equivalent in terms of relative Q structure [*Lees and Lindley*, 1994]. Values of η near 0.65 are typical for many tectonically active areas [*Mitchell*, 1995]. In subduction zones like that in Alaska, measurements show good evidence for frequency dependence of Q in the 0.5–20 Hz range [*Stachnik et al.*, 2004]. In the Alaska subduction zone, both wedge and mantle paths show significantly higher values of η, near 0.4–0.5 in the wedge, and slightly smaller values for slab paths [*Stachnik et al.*, 2004].

Our final velocity spectra fit shows that most of the η values are very small (close to 0) for the southern Puna region (Figure S2), but the η values for the northern part of array (beneath the Cerro Galán region) are as large as 0.8, which is close to the previous estimates (0.65) for tectonically active areas [*Mitchell*, 1995]. We observe a strong correlation between Q and η, which is typical of frequency dependence of Q at higher frequencies. Furthermore, as there is a strong spatial correlation between very high η values and the Cerro Galán region, partial melting could be the potential mechanism for the strong frequency dependence in this area. This strong frequency dependence can be attributed to the dominance of intrinsic over scattering attenuation in the regions dominated by partial melt. These observations suggesting grain boundary relaxation, including partial melting [*Anderson*, 2007], play an important role for seismic wave attenuation in this region. Alternatively, it could also reflect the strong scattering loss due to the spherically symmetric random heterogeneities in the lithosphere [*Yoshimoto et al.*, 1993] around the Cerro Galán region, but this seems less likely.

4. Discussion

The attenuation of seismic waves can be controlled by temperature, water content, cracks (only in the brittle regime), porosity of materials, and partial melt [*Karato and Spetzler*, 1990; *Mitchell*, 1995; *Shankland et al.*, 1981]. Typically, attenuation is primarily sensitive to changes in temperature, water content, and partial melt in the lower crust and uppermost mantle [*Karato and Spetzler*, 1990; *Mitchell*, 1995; *Shankland et al.*, 1981].

4.1. Delamination of South American Lithosphere

The tomographic images clearly show a high Qp and Qs zone with a westward dip beneath the Eastern Cordillera (Figures 6 and 7). This high-Q block could simply be the underthrusted South America continental lithosphere, but the westward dipping feature shows it at least partially detached from the overlain crust. At the same time, given previous geophysical and geochemical observations including evidence of strong attenuation in the uppermost mantle [*Whitman et al.*, 1992, 1996], changes in crustal stresses [*Marrett et al.*, 1994], an intermediate-depth seismicity gap [*Cahill and Isacks*, 1992], and a thin lithosphere [*Whitman et al.*, 1992, 1996] with strong and distinctive volcanic activity [*Kay et al.*, 1994], this high-Q anomaly would seem to be a good candidate for a block of crust/upper mantle that has detached from the overriding South American lithosphere as proposed by *Kay et al.* [1994]. Importantly, the most recent P wave traveltime tomographic images, which use a combined data set that includes data from the PUNA experiment, show a high-velocity anomaly beneath the Cerro Galán [*Bianchi et al.*, 2013]. At the same time, new surface wave tomographic images also show a high-velocity anomaly beneath the same region [*Calixto et al.*, 2013]. Both results appear to correlate with our high-Q zone indicating that the high-velocity zones in these studies can also be interpreted as a delaminated lithospheric block. All of these observations support the presence of a piece of delaminated South American continental lithosphere. The delamination producing this block could have taken place around 2 Ma near the time of the major Cerro Galán eruption at a time of mantle upwelling [*Kay et al.*, 1994, 2011; *Kay and Coira*, 2009].

The depth of the Nazca slab decreases from north to south beneath the plateau in the attenuation images, which is consistent with the steep-to-flat transition of the subducting slab determined by earthquake hypocenters [e.g., *Cahill and Isacks*, 1992; *Mulcahy et al.*, 2010]. The low-Q regions are well correlated with the latest Pliocene (~2 Ma) mafic volcanic activity in the southern Puna plateau [see *Risse et al.*, 2008]. The ~2 Ma Cerro Galán ignimbrite resides above and near the most prominent low-Q anomalies in the crust. The attenuation of the crust and uppermost mantle beneath Cerro Galán is so strong that local S waves are completely blocked for the raypaths going through this part of the lithosphere (Figures 6 and 7), and we were unable to measure S wave amplitudes to calculate t^* for these raypaths. Overall, the lithosphere that was proposed to have delaminated around 2 Ma [*Kay et al.*, 1994] is suggested to be associated with a mantle upwelling above a subduction zone that began to steepen at ~7–6 Ma [*Kay and Coira*, 2009]. The higher temperatures induced by this mantle upwelling are argued to have triggered the melting that led to the eruption of the voluminous Cerro Galán ignimbrite at ~2 Ma [*Folkes et al.*, 2011; *Kay et al.*, 1994, 2011; *Sparks et al.*, 1985] with subsequent partial melting, represented by our low-Q zone, expanding throughout the mantle wedge beneath the Cerro Galán complex.

4.2. Flat-Slab Structure

Another clear observation is the low-Q layer at the southern end of the PUNA array at depths between approximately ~100 and 140 km over the subducting slab, where the slab is shallowing into the flat-slab region (Figure 6, section E-E'; Figure 8, 100 and 120 km sections). We suggest that this low-Q layer could reflect a concentration of fluids just above the slab, possibly along with the initiation of mantle partial melting signaling the beginning of resteepening of the subducting slab in this region [*Kay and Coira*, 2009]. It is important for this argument to note that there is no volcanism younger than 6 to 7 Ma [*Harris et al.*, 2008] directly above this low Qp anomaly and that the overlying mantle and crust shows a high-Q signature indicating little attenuation. This suggests that the low-Q zone currently above the slab is not related to the melting process that generated the volcanism in the overlying Farallon Negro volcanic field at 9.5 to 6 Ma. These late Miocene magmas are best interpreted as being the product of dehydration melting of the mantle wedge as the slab was shallowing in this region [*Kay and Mpodozis*, 2002; *Kay and Coira*, 2009; *Ramos et al.*, 2002; *Sasso and Clark*, 1998].

The situation in section E-E' in Figure 6 contrasts with the prominent low-Q anomalies found beneath the CVZ volcanic arc and in the crust and mantle of the back arc around Cerro Galán (Figure 6, sections A-A' to D-D' and in the northern Puna [*Schurr et al.*, 2003], where the slab dip is much steeper and there is a hot asthenospheric wedge. In these regions, the low-Q zone can extend from the asthenospheric wedge (~200 km) to the upper crust (Figure 6, sections (A-A' to C-C'). An explanation for this large zone of low Q is that the asthenospheric upwelling related with delamination beneath Cerro Galán heats up the surrounding area and speeds up the lithospheric dehydration process in the subducted slab. This dehydration provides a good explanation for the seismicity in the subducting slab to the west, with the heating helping to explain the intermediate depth seismicity gap under the Cerro Galán region to the east [e.g., *Cahill and Isacks*, 1992; *Kay et al.*, 1994; *Mulcahy et al.*, 2010].

The situation under the northern part of the PUNA array is thus quite different from that in the profile near 27.5°S, where the ~50 km thick layer of low-Q mantle wedge above the slab shows no clear connection with any anomaly in the overlying mantle or crust (Figure 6, section E-E'). A further observation in this transect near 27.5°S is that *Bianchi et al.* [2013] report no clear low-velocity Vp anomaly in the uppermost mantle. As even a small fraction of partial melt normally results in abrupt reductions in both Qp and Qs, with the drop in Vp being less pronounced [*Anderson*, 2007], such a contrast provides an argument for dehydration above the descending slab with small amounts of melt in the wedge explaining differences between the Vp and Q tomographic images. Another caveat could be an issue with the resolution of this Vp tomographic image which is on the edge of the network resolution and does not use the local traveltime data.

Of further significance is that the transect near 27.5°S sits in the transition zone from steep subduction under the southern Puna plateau to shallower subduction in the Chilean-Pampean flat-slab region under the Sierras Pampeanas to the south [*Cahill and Isacks*, 1992; *Mulcahy et al.*, 2010]. A general consideration is that dehydration of subducted oceanic crust is argued to occur via metamorphic reactions as temperatures increase and hydrated sediments, oceanic crust, and oceanic uppermost mantle all begin to dehydrate at different temperatures [e.g., *Gerya et al.*, 2009; *Manea and Manea*, 2011]. A flatter subducting plate associated

with a cooler mantle wedge over a cooler subducting slab is thus expected to produce diminished dehydration as the distance increases into the back arc. Such lesser dehydration leading to lesser amounts of melt generation can explain the lack of back-arc volcanism in the region of profile E-E'. At the same time, limited dehydration can explain the relatively thin high-attenuation (low-Q) layer in the mantle wedge above the subducting slab.

As the angle of the subducting slab progressively decreases to the south, the oceanic slab can potentially be near direct contact with the overlaying continental lithosphere or have only a thin layer of asthenosphere as argued by *Smalley and Isacks* [1987] and others [e.g., *Alvarado et al.*, 2009; *Anderson et al.*, 2007; *Porter et al.*, 2012]. Importantly, the surface wave tomographic images in *Porter et al.* [2012] for the flat-slab region show the velocities in the shallow dipping slab increasing eastward as velocities in the overlying mantle wedge decrease, consistent with the prominent seismicity in the slab [*Anderson et al.*, 2007] being due to slab dewatering. This implied dewatering of the slab gradually hydrates the overlying mantle, explaining why lower velocities occur in the overlying mantle wedge in the flat-slab region [*Porter et al.*, 2012].

Returning to the section at 27.5°S (Figure 6, section E-E'), the presence of fluids just above the flat slab could help to facilitate some magma generation [*Rüpke et al.*, 2004]. Evidence for a hotter mantle beneath this region than over the flat slab farther south comes from uplift data and the basin formation history in this area, which appear to reflect formation over a relatively hotter and more actively uplifting region as compared to the flat-slab region farther south [e.g., *Dávila et al.*, 2012]. In particular, a compilation of fission track length and ages by *Dávila and Carter* [2013] shows that late Neogene uplift rates require a higher mantle wedge temperature in the region of the Pipanaco basin over the 27.5°S transect. At the same time, it is important to note that very young back-arc volcanism (<1 Ma) does occur in the Pasto Ventura region, which is only ~60–70 km to the north.

Since large P and S wave velocity anomalies are not observed near 27.5°S [*Bianchi et al.*, 2013; *Calixto et al.*, 2013, respectively], the simplest explanation could be that melt generation in this region has just reinitiated after a late Miocene to Pliocene gap and is in the very early stages. This magma generation could be associated with the initial resteepening of the subducting slab in this area, and thus the low-Q zone could also reflect a combination of decompression melting over a steepening slab and flux melting from fluids originating from the heated slab. Overall, the fluids released from the dehydration process in the modern setting are unlikely to be able to migrate upward efficiently by porous flow and are thus potentially trapped above the slab contributing to the low-Q anomaly. A colder slab in this region than to the north may prevent the generation of sufficient fluid to set up the conditions for melting in the wedge. Thus, we conclude that both fluids and the earliest stages of magma generation could produce this very highly attenuating layer just above the slab at the transition from steep to flat-slab subduction.

The contrast between the prominent low-Q anomalies found beneath the magmatic arc and the back arc in the crust and mantle in the northern Puna [e.g., *Schurr et al.*, 2003] and around Cerro Galán (Figure 6, sections A-A' and B-B'), where the slab is more steeply dipping and there is a hot asthenospheric wedge, and the region of the thinner prominent low-Q layer above the more shallow dipping subducting slab near 27.5°S beneath the southernmost part of the array (Figure 6, section E-E') shows a clear transition in the lateral style of the mechanism of the generation of the low-Q anomaly. This mechanism difference reflects a change from prominent partial melting by delamination induced asthenospheric upwelling in the north to gradual dehydration with or without small volume partial melting related to the early stages of slab resteepening in the south.

5. Conclusions

We observe an extensive low-Q region beneath the Cerro Galán caldera region next to a westward dipping high-Q zone at 50–150 km depth beneath the Eastern Cordillera to the east, which we interpret as indicating the presence of a piece of delaminated South American lithosphere. This extensive low-Q zone, which is between the Nazca slab and South American lithosphere, extends from the northern margin of the array at 25°S to around 27.5°S, where it vanishes. From a west to east perspective, the low-Q zone extends farther to the west in the crust and uppermost mantle at the southern end of the array where the frontal volcanic arc is most active. In detail, the low-Q zone extends for over ~100 km in depth above the slab under the back arc in the northern part of the array but becomes a thinner sheet with a thickness of <50 km under the South

American continental lithosphere in the back arc to the south. The transition from the north to the south reflects different origins for the low-Q anomalies in the two regions. In the north, we interpret the low-Q anomaly dominantly reflecting mantle upwelling and partial melting after delamination of the South American continental lithosphere under the Cerro Galán region. In contrast, in the south we interpret the thinner low-Q anomaly as reflecting dehydration of the subducted oceanic slab or as the very early stages of melt generation in a young asthenospheric wedge as the very northern edge of the flat slab has begun to steepen. We suggest that it is most likely that both processes are occurring in the south. In summary, we see dramatic north to south variations in the Q structure and this change strongly correlates with the delamination of continental lithosphere beneath Cerro Galán combined with the change in the angle of subduction.

References

Allmendinger, R. W. (1986), Tectonic development, southeastern border of the Puna plateau, northwestern Argentine Andes, *Geol. Soc. Am. Bull.*, *97*(9), 1070–1082.

Allmendinger, R. W., T. E. Jordan, S. M. Kay, and B. L. Isacks (1997), The evolution of the Altiplano-Puna plateau of the central Andes, *Annu. Rev. Earth Planet. Sci.*, *25*(1), 139–174.

Alvarado, P., M. Pardo, H. Gilbert, S. Miranda, M. Anderson, M. Saez, and S. Beck (2009), Flat-slab subduction and crustal models for the seismically active Sierras Pampeanas region of Argentina, *Geol. Soc. Am. Mem.*, *204*, 261–278.

Anderson, D. L. (2007), *New Theory of the Earth*, 2nd ed., Cambridge Univ. Press, New York.

Anderson, M., P. Alvarado, G. Zandt, and S. Beck (2007), Geometry and brittle deformation of the subducting Nazca Plate, Central Chile and Argentina, *Geophys. J. Int.*, *171*(1), 419–434.

Barazangi, M., and B. L. Isacks (1976), Spatial distribution of earthquakes and subduction of the Nazca plate beneath South America, *Geology*, *4*(11), 686–692.

Beck, S. L., and G. Zandt (2002), The nature of orogenic crust in the central Andes, *J. Geophys. Res.*, *107*(B10), 2230, doi:10.1029/2000JB000124.

Bianchi, M., et al. (2013), Teleseismic tomography of the southern Puna plateau in Argentina and adjacent regions, *Tectonophysics*, *586*, 65–83.

Brune, J. N. (1970), Tectonic stress and the spectra of seismic shear waves from earthquakes, *J. Geophys. Res.*, *75*(26), 4997–5009.

Cahill, T., and B. L. Isacks (1992), Seismicity and shape of the subducted Nazca plate, *J. Geophys. Res.*, *97*(B12), 17,503–17,529.

Calixto, F. J., E. Sandvol, S. Kay, P. Mulcahy, B. Heit, X. Yuan, B. Coira, D. Comte, and P. Alvarado (2013), Velocity structure beneath the southern Puna plateau: Evidence for delamination, *Geochem. Geophys. Geosyst.*, *14*, 4292–4305, doi:10.1002/ggge.20266.

Coira, B., and S. M. Kay (1993), Implications of Quaternary volcanism at Cerro Tuzgle for crustal and mantle evolution of the Puna plateau, central Andes, Argentina, *Contrib. Mineral. Petrol.*, *113*(1), 40–58.

Coira, B., S. M. Kay, and J. Viramonte (1993), Upper Cenozoic magmatic evolution of the Argentine Puna—A model for changing subduction geometry, *Int. Geol. Rev.*, *35*(8), 677–720.

Davidson, J., and S. Silva (1995), Late Cenozoic magmatism of the Bolivian Altiplano, *Contrib. Mineral. Petrol.*, *119*(4), 387–408.

Dávila, F. M., and A. Carter (2013), Exhumation history of the Andean broken foreland revisited, *Geology*, *41*(4), 443–446.

Dávila, F. M., M. E. Giménez, J. C. Nóbile, and M. P. Martínez (2012), The evolution of the high-elevated depocenters of the northern Sierras Pampeanas (ca. 28°SL), Argentine broken foreland, south-central Andes: The Pipanaco Basin, *Basin Res.*, *24*(6), 615–636.

Eberhart-Phillips, D., and M. Chadwick (2002), Three-dimensional attenuation model of the shallow Hikurangi subduction zone in the Raukumara Peninsula, New Zealand, *J. Geophys. Res.*, *107*(B2), 2033, doi:10.1029/2000JB000046.

England, P., and G. Houseman (1989), Extension during continental convergence, with application to the Tibetan Plateau, *J. Geophys. Res.*, *94*, 17,561–17,579.

Febrer, J., B. Baldis, J. Gasco, M. Mamani, and C. Pomposielo (1982), La anomalia geothermica Calchaqui en el noroeste de Argentina: Un nuevo proceso geodinamica asociada a la subduccion de la placa de Nazca. Quinto Congreso Latinoamericano de Geologia, Argentina. Actas III, 705-718.

Folkes, C., H. Wright, R. Cas, S. de Silva, C. Lesti, and J. Viramonte (2011), A re-appraisal of the stratigraphy and volcanology of the Cerro Galán volcanic system, NW Argentina, *Bull. Volcanol.*, *73*(10), 1427–1454.

Gardeweg, M., J. Clavero, C. Mpodozis, C. Perez de Arce, and M. Villeneuve (2000), El Macizo Tres Cruces: Un complejo volcánico longevo y potencialmente activo en la Alta Cordillera de Copiapó, Chile. Actas IX Congreso Geológico Chileno, Simposio Geología y Recursos Minerales de los Andes Centrales, avances del Proyecto Multinacional Andino, MAP, Vol II, p.291-295.

Gerya, T. V., D. Fossati, C. Cantieni, and D. Seward (2009), Dynamic effects of aseismic ridge subduction: numerical modelling, *Eur. J. Mineral.*, *21*(3), 649–661.

Goss, A. R., S. M. Kay, C. Mpodozis, and B. S. Singer (2009), The Incapillo Caldera and Dome Complex (~28°S, central Andes): A stranded magma chamber over a dying arc, *J. Volcanol. Geotherm. Res.*, *184*(3–4), 389–404.

Harris, A., W. J. Dunlap, P. Reiners, C. Allen, D. Cooke, N. White, I. Campbell, and S. Golding (2008), Multimillion year thermal history of a porphyry copper deposit: Application of U–Pb, 40Ar/39Ar and (U–Th)/He chronometers, Bajo de la Alumbrera copper–gold deposit, Argentina, *Miner. Deposita*, *43*(3), 295–314.

Heit, B., I. Koulakov, G. Asch, X. Yuan, R. Kind, I. Alcocer-Rodriguez, S. Tawackoli, and H. Wilke (2008), More constraints to determine the seismic structure beneath the Central Andes at 21°S using teleseismic tomography analysis, *J. South Am. Earth Sci.*, *25*(1), 22–36.

Isacks, B. L. (1988), Uplift of the central Andean plateau and bending of the Bolivian orocline, *J. Geophys. Res.*, *93*(B4), 3211–3231.

Jordan, T. E., B. L. Isacks, R. W. Allmendinger, J. A. Brewer, V. A. Ramos, and C. J. Ando (1983), Andean tectonics related to geometry of subducted Nazca plate, *Geol. Soc. Am. Bull.*, *94*(3), 341–361.

Karato, S., and H. Spetzler (1990), Defect microdynamics in minerals and solid-state mechanisms of seismic wave attenuation and velocity dispersion in the mantle, *Rev. Geophys.*, *28*(4), 399–421.

Kay, S. M., and J. M. Abbruzzi (1996), Magmatic evidence for Neogene lithospheric evolution of the central Andean "flat-slab" between 30°S and 32°S, *Tectonophysics*, *259*(1–3), 15–28.

Kay, S. M., and B. L. Coira (2009), Shallowing and steepening subduction zones, continental lithospheric loss, magmatism, and crustal flow under the central Andean Altiplano-Puna Plateau, *Geol. Soc. Am. Mem.*, *204*, 229–259.

Kay, R. W., and S. M. Kay (1993), Delamination and delamination magmatism, *Tectonophysics*, *219*(1–3), 177–189.

Kay, S. M., and C. Mpodozis (2002), Magmatism as a probe to the Neogene shallowing of the Nazca plate beneath the modern Chilean flat-slab, *J. South Am. Earth Sci.*, *15*(1), 39–57.

Kay, S. M., B. Coira, and J. Viramonte (1994), Young mafic back arc volcanic rocks as indicators of continental lithospheric delamination beneath the Argentine Puna plateau, central Andes, *J. Geophys. Res.*, *99*(B12), 24,323–24,339.

Kay, S. M., B. L. Coira, P. J. Caffe, and C.-H. Chen (2010), Regional chemical diversity, crustal and mantle sources and evolution of central Andean Puna plateau ignimbrites, *J. Volcanol. Geotherm. Res.*, *198*(1–2), 81–111.

Kay, S., B. Coira, G. Wörner, R. Kay, and B. Singer (2011), Geochemical, isotopic and single crystal ^{40}Ar/^{39}Ar age constraints on the evolution of the Cerro Galán ignimbrites, *Bull. Volcanol.*, *73*(10), 1487–1511.

Kay, S. M., C. Mpodozis, and M. Gardeweg (2013), Magma sources and tectonic setting of central Andean andesites (25.5°–28°S) related to crustal thickening, forearc subduction erosion and delamination, in *Orogenic Andesites and Crustal Growth*, vol. 385, edited by A. Gomez-Tuena, S. M. Straub, and G. F. Zellmer, p. 32, Geol. Soc. London Spec. Pub., London, doi:10.1144/SP385.11.

Lees, J., and G. Lindley (1994), Three-dimensional attenuation tomography at Loma Prieta: Inversion of t* for Q, *J. Geophys. Res.*, *99*(B4), 6843–6863.

Luo, G., and M. Liu (2009), Why short-term crustal shortening leads to mountain building in the Andes, but not in Cascadia?, *Geophys. Res. Lett.*, *36*, L08301, doi:10.1029/2009GL037347.

Manea, V., and M. Gurnis (2007), Subduction zone evolution and low viscosity wedges and channels, *Earth Planet. Sci. Lett.*, *264*(1–2), 22–45.

Manea, V., and M. Manea (2011), Flat-slab thermal structure and evolution beneath central Mexico, *Pure Appl. Geophys.*, *168*(8), 1475–1487.

Marrett, R. A., R. W. Allmendinger, R. N. Alonso, and R. E. Drake (1994), Late Cenozoic tectonic evolution of the Puna Plateau and adjacent foreland, northwestern Argentine Andes, *J. South Am. Earth Sci.*, *7*(2), 179–207.

Mitchell, B. J. (1995), Anelastic structure and evolution of the continental crust and upper mantle from seismic surface wave attenuation, *Rev. Geophys.*, *33*(4), 441–462.

Molnar, P., P. England, and J. Martinod (1993), Mantle dynamics, uplift of the Tibetan Plateau, and the Indian monsoon, *Rev. Geophys.*, *31*(4), 357–396.

Mulcahy, P., C. Chen, S. M. Kay, L. D. Brown, P. Alvarado, E. Sandvol, B. Heit, and X. Yuan (2010), The southern Puna seismic experiment: Shape of the subducting Nazca plate, areas of concentrated mantle and crustal earthquakes, and crustal focal mechanisms, Abstract T11A-2050 presented at 2010 Fall Meeting, AGU, San Francisco, Calif.

Myers, S. C., S. Beck, G. Zandt, and T. Wallace (1998), Lithospheric-scale structure across the Bolivian Andes from tomographic images of velocity and attenuation for *P* and *S* waves, *J. Geophys. Res.*, *103*(B9), 21,233–21,252.

Oncken, O., D. Hindle, J. Kley, K. Elger, P. Victor, and K. Schemmann (2006), Deformation of the central Andean upper plate system—Facts, fiction, and constraints for plateau models, in *The Andes*, edited by O. Oncken et al., pp. 3–27, Springer, Berlin, Heidelberg.

Park, J., C. Lindberg, and F. Vernon III (1987), Multitaper spectral analysis of high-frequency seismograms, *J. Geophys. Res.*, *92*(B12), 12,675–12,684.

Pilger, R. H. (1981), Plate reconstructions, aseismic ridges, and low-angle subduction beneath the Andes, *Geol. Soc. Am. Bull.*, *92*(7), 448–456.

Porter, R., H. Gilbert, G. Zandt, S. Beck, L. Warren, J. Calkins, P. Alvarado, and M. Anderson (2012), Shear wave velocities in the Pampean flat-slab region from Rayleigh wave tomography: Implications for slab and upper mantle hydration, *J. Geophys. Res.*, *117*, B11301, doi:10.1029/2012JB009350.

Ramos, V. A., E. O. Cristallini, and D. J. Pérez (2002), The Pampean flat-slab of the central Andes, *J. South Am. Earth Sci.*, *15*(1), 59–78.

Risse, A., R. B. Trumbull, B. Coira, S. M. Kay, and P. v. d. Bogaard (2008), ^{40}Ar/^{39}Ar geochronology of mafic volcanism in the back-arc region of the southern Puna plateau, Argentina, *J. South Am. Earth Sci.*, *26*(1), 1–15.

Rüpke, L. H., J. P. Morgan, M. Hort, and J. A. D. Connolly (2004), Serpentine and the subduction zone water cycle, *Earth Planet. Sci. Lett.*, *223*(1–2), 17–34.

Sasso, A., and A. Clark (1998), The Farallón Negro Group, northwest Argentina: Magmatic, hydrothermal and tectonic evolution and impli-cations for Cu-Au metallogeny in the Andean back-arc: SEG (Society of Economic Geologist) Newsletter, no. 34, p. 1, 8-18.

Scherbaum, F. (1990), Combined inversion for the three-dimensional Q structure and source parameters using microearthquake spectra, *J. Geophys. Res.*, *95*(B8), 12,423–12,438.

Schurr, B., G. Asch, A. Rietbrock, R. Trumbull, and C. Haberland (2003), Complex patterns of fluid and melt transport in the central Andean subduction zone revealed by attenuation tomography, *Earth Planet. Sci. Lett.*, *215*(1–2), 105–119.

Schurr, B., A. Rietbrock, G. Asch, R. Kind, and O. Oncken (2006), Evidence for lithospheric detachment in the central Andes from local earthquake tomography, *Tectonophysics*, *415*(1–4), 203–223.

Shankland, T. J., R. J. Connell, and H. S. Waff (1981), Geophysical constraints on partial melt in the upper mantle, *Rev. Geophys.*, *19*(3), 394–406.

Smalley, R. F., and B. L. Isacks (1987), A high-resolution local network study of the Nazca plate Wadati-Benioff zone under western Argentina, *J. Geophys. Res.*, *92*(B13), 13,903–13,912.

Sparks, R. S. J., P. W. Francis, R. D. Hamer, R. J. Pankhurst, L. O. O'Callaghan, R. S. Thorpe, and R. Page (1985), Ignimbrites of the Cerro Galan caldera, NW Argentina, *J. Volcanol. Geotherm. Res.*, *24*(3–4), 205–248.

Stachnik, J. C., G. A. Abers, and D. H. Christensen (2004), Seismic attenuation and mantle wedge temperatures in the Alaska subduction zone, *J. Geophys. Res.*, *109*, B10304, doi:10.1029/2004JB003018.

Tassara, A. (2005), Interaction between the Nazca and South American plates and formation of the Altiplano–Puna plateau: Review of a flexural analysis along the Andean margin (15°–34°S), *Tectonophysics*, *399*(1–4), 39–57.

Thurber, C., and D. Eberhart-Phillips (1999), Local earthquake tomography with flexible gridding, *Comput. Geosci.*, *25*(7), 809–818.

Wang, Y.-J., K-F. Ma, F. Mouthereau, and D. Eberhart-Phillips (2010), Three-dimensional Qp and Qs tomography beneath Taiwan orogenic belt: Implications for tectonic and thermal structure, *Geophys. J. Int.*, *180*(2), 891–910.

Whitman, D., B. L. Isacks, J.-L. Chatelain, J.-M. Chiu, and A. Perez (1992), Attenuation of high-frequency seismic waves beneath the central Andean plateau, *J. Geophys. Res.*, *97*(B13), 19,929–19,947.

Whitman, D., B. L. Isacks, and S. M. Kay (1996), Lithospheric structure and along-strike segmentation of the central Andean plateau: Seismic Q, magmatism, flexure, topography and tectonics, *Tectonophysics*, *259*(1–3), 29–40.

Yáñez, G. A., C. R. Ranero, R. von Huene, and J. Díaz (2001), Magnetic anomaly interpretation across the southern central Andes (32°–34°S): The role of the Juan Fernández Ridge in the late Tertiary evolution of the margin, *J. Geophys. Res.*, *106*(B4), 6325–6345.

Yoshimoto, K., H. Sato, and M. Ohtake (1993), Frequency-dependent attenuation of *P* and *S* waves in the Kanto area, Japan, based on the coda-normalization method, *Geophys. J. Int.*, *114*(1), 165–174.